Sulfated Cellulose Nanocrystals into Piezoelectricity- Introducing a New Material into Piezoelectric Energy Harvesting and Smart Strain Sensing for

Advanced Composites and Hybrid Materials (2026) 9:205
https://doi.org/10.1007/s42114-026-01819-2

RESEARCH

Sulfated Cellulose Nanocrystals into Piezoelectricity- Introducing a New Material into Piezoelectric Energy Harvesting and Smart Strain Sensing for Health Monitoring Applications

Sujith Lal[1] · Omkar Y. Pawar[2] · Anja Lund[3] · Ergang Wang[4] · Sooman Lim[2] · Byungil Hwang[1]

Received: 8 January 2026 / Revised: 13 April 2026 / Accepted: 17 April 2026

Abstract

The development of multifunctional, flexible, and sustainable wearable electronics is critical for the advancement of next-generation smart systems. In this paper, a dual-functional, self-powered device capable of both piezoelectric energy harvesting and high-sensitivity strain sensing is reported. This device was fabricated using sulfated cellulose nanocrystals (SCNCs) derived from waste tissue. These SCNCs were integrated with carbon nanotubes (CNTs) and polyvinyl alcohol (PVA) and supported on biodegradable mulberry paper (MP). It was found that sulfation enhanced the surface charge density, crystallinity, and dipole alignment of the CNCs, thereby significantly improving the piezoelectric performance confirmed with theoretical simulation such as DFT, COMSOL Multiphysics simulation, piezobased dielectric studies and characterization experiments. Based on the experimental demonstration, the optimized composite device exhibited an open-circuit voltage of 6–8 V and short-circuit current of 120–150 nA under mechanical deformation. Furthermore, it demonstrated a rapid response (0.5–2 s) and high sensitivity of more than 80% in detecting physiological motions, such as the human pulse, finger bending, and neck movements. In addition to energy harvesting, the device exhibited reliable strain-sensing capabilities when mounted on various body parts. Practical demonstrations included integration with Arduino-based circuits for real-time applications, such as smart doorbell systems and safety line-crossing detection, wherein electrical signals are converted into wireless alerts. This combination of sustainability, flexibility, mechanical robustness, and dual functionality highlights the potential of the developed SCNC-based platform for use in self-powered wearable electronics with promising implications for health monitoring, interactive interfaces, and eco-friendly smart devices.

Keywords Sulfated CNC · Piezoelectric · Strain sensor · Wearable sensor · Health monitoring · DFT · COMSOL

✉ Ergang Wang
ergang@chalmers.se

✉ Sooman Lim
smlim@jbnu.ac.kr

✉ Byungil Hwang
bihwang@cau.ac.kr

[1] School of Integrative Engineering, Chung-Ang University, Seoul 06974, Republic of Korea

[2] Graduate School of Flexible and Printable Electronics, LANL-JBNU Engineering Institute- Korea, Jeonbuk National University, Jeonju, Republic of Korea

[3] Department of Polymers, Fibers and Composites, Fiber development, RISE Research Institutes of Sweden, Argongatan 30, Mölndal SE-431 53, Sweden

[4] Department of Chemistry and Chemical Engineering, Chalmers University of Technology, Göteborg SE-412 96, Sweden

1 Introduction

Self-powered sensing systems represent a transformative approach to the development of next-generation wearable electronics, enabling devices to operate independently without relying on external power supplies [1, 2]. These systems harvest ambient mechanical energy and simultaneously detect external stimuli [3–6], offering energy autonomy and real-time monitoring capabilities [7–9]. Among the various energy harvesting strategies reported to date, piezoelectric systems have garnered particular attention owing to their ability to convert biomechanical energy into an electrical output via internal dipole polarization [10, 11]. Their lightweight nature, structural simplicity, and compatibility with flexible form factors further enhance their suitability for wearable applications [12–14]. One unique advantage

Published online: 27 April 2026

of piezoelectric materials lies in their dual functionality as both active sensors and energy harvesters, rendering them ideal candidates for real-time physiological monitoring, emergency detection, and human–machine interfaces [15, 16]. Recent advances in low-power wireless transmission technologies have accelerated the practical integration of these systems into mobile platforms, thereby expanding their applicability in smart healthcare and personalized medicine [9, 17, 18]. Despite substantial progress in this area, the realization of fully integrated, high-performance, and self-powered sensors under real-world operating conditions remains limited by material inefficiencies, fabrication complexity, and durability concerns.

Various functional materials and composite designs have been explored to enhance the piezoelectric performances and sensing capabilities of wearable systems [19, 20]. For instance, Janus nanofiber membranes [21], hybrid piezoelectric–piezoresistive sensors [18], and MXene-integrated composites [22, 23] and metal organic frameworks (MOFs) have demonstrated promising characteristics such as improved flexibilities and sensitivities [24]. However, these systems often suffer from suboptimal output voltages (<3 V), complicated synthetic processes, poor long-term environmental stabilities, or the incorporation of materials with limited biocompatibility characteristics. For example, although MXenes exhibit excellent conductivities and electromechanical properties, they are susceptible to oxidation and structural degradation, particularly in aqueous or humid conditions, which pose significant obstacles to their deployment in wearable or implantable platforms [25]. Despite the fact that contemporary approaches offer promising advancements, conventional inorganic piezoelectric materials, such as lead zirconate titanate (PZT) [26], zinc oxide [27], barium titanate [28], and potassium sodium niobate [29] still represent benchmarks in terms of their high energy-conversion efficiencies. Nonetheless, these traditional materials have drawbacks in the context of wearable applications, including toxicity concerns (e.g., lead in PZT), environmental issues, complicated processing methods, and mechanical rigidity [26, 30].

In response to these limitations, an increasing number of studies have focused on the development of biocompatible and sustainable materials. For instance, cellulose nanocrystals (CNCs) derived from natural biomass have emerged as promising alternatives because of their nontoxic nature, biodegradability, affordability, and exceptional mechanical properties [31]. While CNCs inherently exhibit piezoelectric properties attributed to their Iβ crystalline structure, their standalone performances typically remain inadequate for practical sensing or energy harvesting applications [32]. Consequently, CNCs are often integrated into polymer-based composites (e.g., polyvinylidene fluoride, PVDF), wherein the CNCs enhance the mechanical integrity and sustainability, while the polymer predominantly contributes to the piezoelectric response [33, 34]. However, such polymer-based composites encounter various issues, such as limited biodegradabilities, reduced environmental compatibilities, and a dependency on synthetic polymers, all of which compromise the overall sustainability and biocompatibility of the final device [35].

To overcome these limitations and realize a truly eco-friendly, high-performance, dual-functional piezoelectric platform, this study explored a new strategy of chemical modification of CNCs by controlled sulfation via sulfuric acid hydrolysis method. Sulfate ($-O-SO_3^-$) groups on CNC surface increase the surface charge density, enhance dispersibility, promote dipole alignment, and improve the overall crystallinity, with the overall aim of boosting the piezoelectric output. The sulfated CNCs (SCNCs) are subsequently incorporated into a composite system with carbon nanotubes (CNTs) and polyvinyl alcohol (PVA) to provide efficient charge transport and an improved mechanical robustness. Furthermore, to enhance the device sustainability, SCNCs are synthesized from waste tissue sources, and mulberry paper (MP), which is a biodegradable and mechanically stable substrate with an excellent compatibility, is employed to support the composite. The performance of the resulting device is then investigated, including its open-circuit voltage, sensitivity to subtle physiological signals (e.g., human pulses), and strain sensing behaviors across various body motions. Overall, this study aims to introduce a green and scalable fabrication strategy, while also advancing the design of self-powered, dual-functional wearable electronics capable of addressing current limitations in energy autonomy, sensitivity, and environmental compatibility.

2 Results and discussion

2.1 Structural, morphological, and chemical characteristics

The PVA/CNT@SCNC composite was fabricated via sulfuric acid hydrolysis, followed by a dip-coating process, in which the CNTs acted as conductive pathways and the PVA served as a polymeric binder. As shown in Fig. 1a, the composite layer was symmetrically coated on both sides of the mulberry paper substrate to form a well-defined sandwich-like architecture. SEM observations (Fig. 1b) revealed a highly porous, interconnected fibrous network, which promotes efficient charge transport, while preserving the mechanical flexibility and structural integrity. Elemental mapping (Fig. 1b1) confirmed the uniform spatial

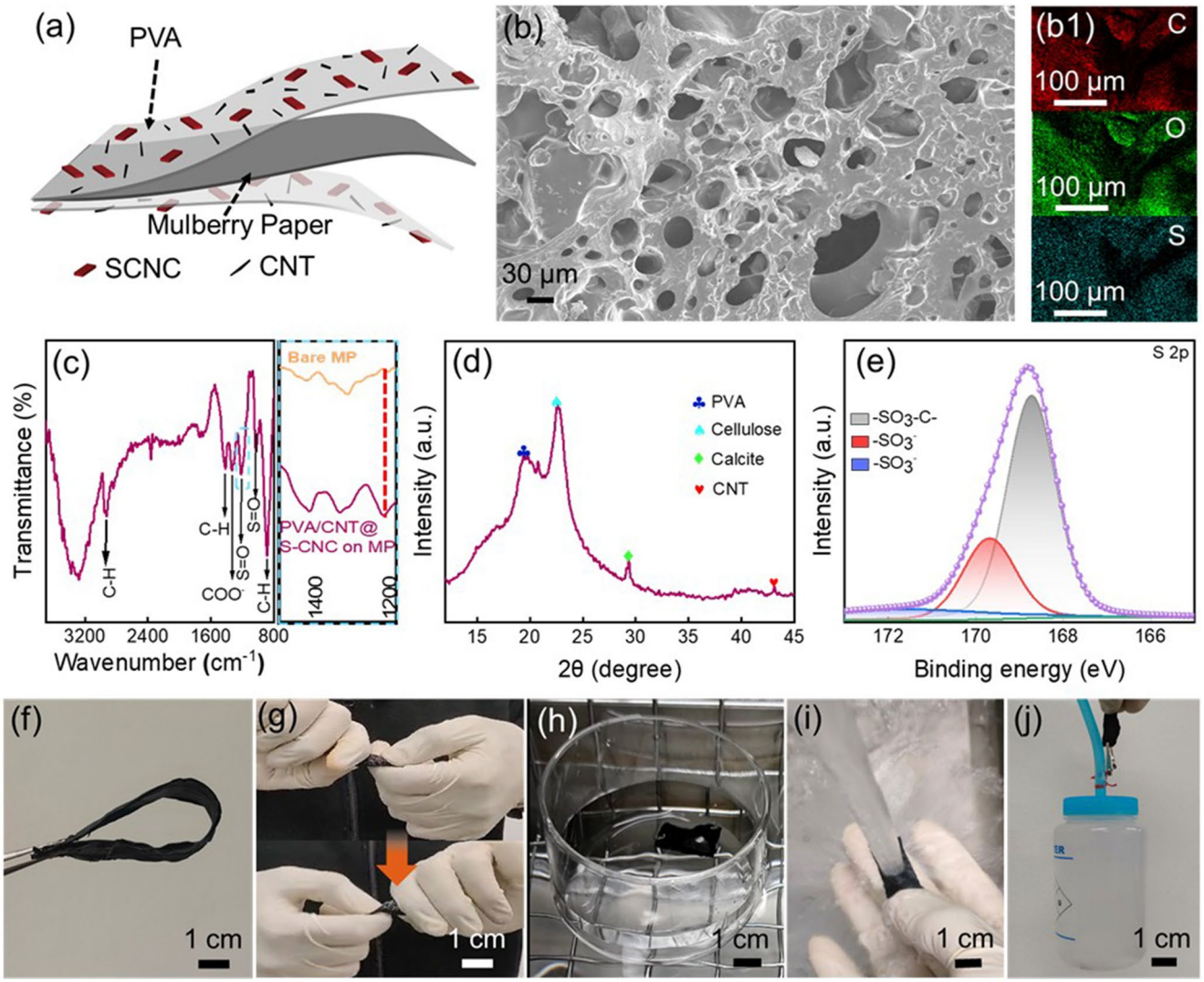

Fig. 1 (**a**) Graphical demonstration of the fabricated device having a coating of SCNCs integrated with the PVA and CNT composite. (**b**) Obtained morphology of the device, as observed using FE-SEM. (b1) Elemental mapping images of carbon, oxygen, and sulfur. (**c**) FTIR spectrum of the device. (**d**) XRD pattern of the device. (**e**) XPS results for sulfur components. Photographic images of the device under (**f**) bending, (**g**) twisting, (**h**) sonicating, (**i**) washing, and (**j**) mechanical hanging using a weight of 500 g

distributions of carbon, oxygen, and sulfur throughout the matrix, indicating the homogeneous incorporation of SCNC and the formation of a continuous, electrochemically active interface conducive to an enhanced charge-carrier mobility.

FTIR spectroscopy (Fig. 1c) verified the successful sulfation of cellulose, as evidenced by the characteristic S=O stretching vibrations observed at 1033 and 1212 cm^{-1} [36–38]. In contrast, the FTIR spectrum of the pristine MP (Fig. 1c) lacked these peaks, confirming that sulfonic functional groups were introduced during the modification process. The observation of a weak C–H stretching vibration at 2924 cm^{-1} further suggests chemical alteration of the carbon backbone [39], while the additional peaks observed at 881 cm^{-1} (C–H out-of-plane bending, indicative of cellulose I crystallinity), 1340 cm^{-1} (COO^{-}) [40], and 1412 cm^{-1} (C–H and –OH bending) [41], provide further evidence for structural and chemical modification of the cellulose matrix. Furthermore, the broad absorption band observed near 3300cm^{-1} was attributed to the hydroxyl groups, indicative of an enhanced surface polarity and an increased charge density.

XRD (Fig. 1d) revealed a prominent diffraction peak at 22.5°, corresponding to the (002) plane of cellulose I, and confirming that the crystalline nature of the cellulose framework was retained; notably, this is an essential feature of piezoelectric functionality [42]. The additional peaks observed at 19.1° and 40.9° were attributed to the (101) plane and higher-order reflections of the semi-crystalline PVA domains, respectively [43], demonstrating the successful integration and preservation of both cellulose I and PVA

within the hybrid composite. Furthermore, a peak obtained at 43° indicates a presence of graphite phase of CNT with plane (100) [44] while a minor peak at 29.3° depicts the basement of calcite presence in the mulberry tree-based cellulose [45]. No new peaks were observed, suggesting that PVA and CNTs were physically embedded with SCNCs into the cellulose backbone.

XPS (Fig. 1e) further confirmed the incorporation of sulfate functionalities. More specifically, the distinct S 2p peaks at 168.7, 169.95, and 170.41 eV are consistent with oxidized sulfate species [46]. The C 1 s spectrum shows peaks at 284.4 eV (C–C) and 286.0 eV (C–OH), while the O 1 s peaks at 532.0 and 532.3 eV correspond to C = O and hydroxyl oxygen environments, respectively [47, 48]. Based on these combined findings, along with the additional spectral data shown in Figure S1, the successful incorporation of sulfated CNCs was confirmed, along with the preservation of key functional groups. Collectively, these sulfate functional groups are expected to contribute to an enhanced dipole alignment and piezoelectric potential within the composite. Therefore, the zeta potential of sulfated and non-sulfated CNC was measured, as shown in Figure S2. After sulfation, the surface charge significantly increased from −2.46 mV to −18.21 mV, confirming the successful introduction of negatively charged functional groups and an enhanced surface charge density. This increased charge density is expected to facilitate stronger dipole formation and alignment under mechanical stimuli, thereby contributing to the improved piezoelectric performance of the material.

The mechanical resilience of the device was subsequently demonstrated through several deformation tests. The composite withstood bending (Fig. 1f), twisting (Fig. 1g), ultrasonic agitation (Fig. 1h), and high-pressure water impact (Fig. 1i) without any observable delamination or breakage. Moreover, the device sustained a static load of 500 g without structural failure (Fig. 1j), demonstrating its excellent mechanical robustness and suitability for use in flexible and wearable electronics.

2.2 Theoretical investigation of enhanced electric potential/piezoelectricity of SCNC using DFT and COMSOL

To elucidate the molecular origin of the enhanced piezoelectric performance in SCNCs, comprehensive DFT calculations were performed using the PBE-D3 functional. A 1 × 1 × 2 supercell of cellulose Iβ was constructed, in which three surface hydroxyl groups were systematically replaced with SO_3^-/Na^+ pairs to model the sulfated structure (see Methods for computational details) (Fig. 2a). Charge redistribution analysis revealed significant electron transfer of approximately 0.38 |e| per SO_3^- group from the glucose backbone to the sulfate moieties (Fig. 2b). This charge migration establishes strong local dipoles aligned with the crystallographic c-axis, fundamentally altering the material's electrostatic landscape. The resulting electrostatic potential gradient along the chain axis increased dramatically from 0.20 V nm^{-1} in pristine CNC to 0.42 V nm^{-1} in SCNC (Fig. 2c), representing a two-fold enhancement. This charge density difference plot reveals that pristine CNC exhibits relatively symmetric charge distribution with localized electron accumulation and depletion regions, resulting in a weak dipole formation. In contrast, the SCNC shows pronounced charge separation, indicating enhanced dipole polarization which directly contributes to the improved piezoelectric response. Further support provided by Bader charge analysis confirmed the significant polarization by quantitative charge analysis with sulfur atoms carrying −0.59 e while maintaining positive charges (+0.30 e) on backbone carbons (Fig. 2 d). This pronounced charge separation translates to a 3.4-fold increase in the calculated unit-cell dipole moment, from 3.2 D in pristine CNC to 11.0 D in SCNC. Electronic structure calculations revealed that sulfation introduces localized states approximately 2.8 eV below the conduction band edge without compromising the wide band gap (~4.9 eV) essential for piezoelectric functionality (Fig. 2e). This confirms that the SO3- functional groups act as strong electron-withdrawing centers, generating internal electric fields and promoting dipole alignment. These sulfate-derived states enhance the material's electronic polarizability, contributing to the improved electromechanical response. These DFT results show that sulfation boosts piezoelectricity by creating stronger dipoles through charge transfer, tripling the unit-cell dipole moment, and enhancing polarizability—providing the molecular basis for our devices' improved performance.

To investigate and elucidate the structural changes induced by sulfation and their influence on enhancing the piezoelectric properties of the material, we carried out a coupled mechanical–electrical simulation study using COMSOL Multiphysics. A 3D rectangular slab (2 cm × 2 cm × 0.1 cm) was modeled as the base material to compare the performance of pristine CNC and SCNCs. The electric potential (V) was analyzed by integrating solid mechanics with electrostatics. The detailed governing equations, boundary conditions, and simulation parameters are provided in Supporting Information (Section **S1**). The material properties used for the COMSOL simulations of SCNC are summarized in Table S1.

Figure 2f illustrates the variation in surface electric potential when a mechanical pressure of 1 MPa is applied to pristine CNC. The simulation results reveal that CNC generates an electric potential of approximately 0.13 V under this load, whereas sulfated CNCs exhibit significantly enhanced

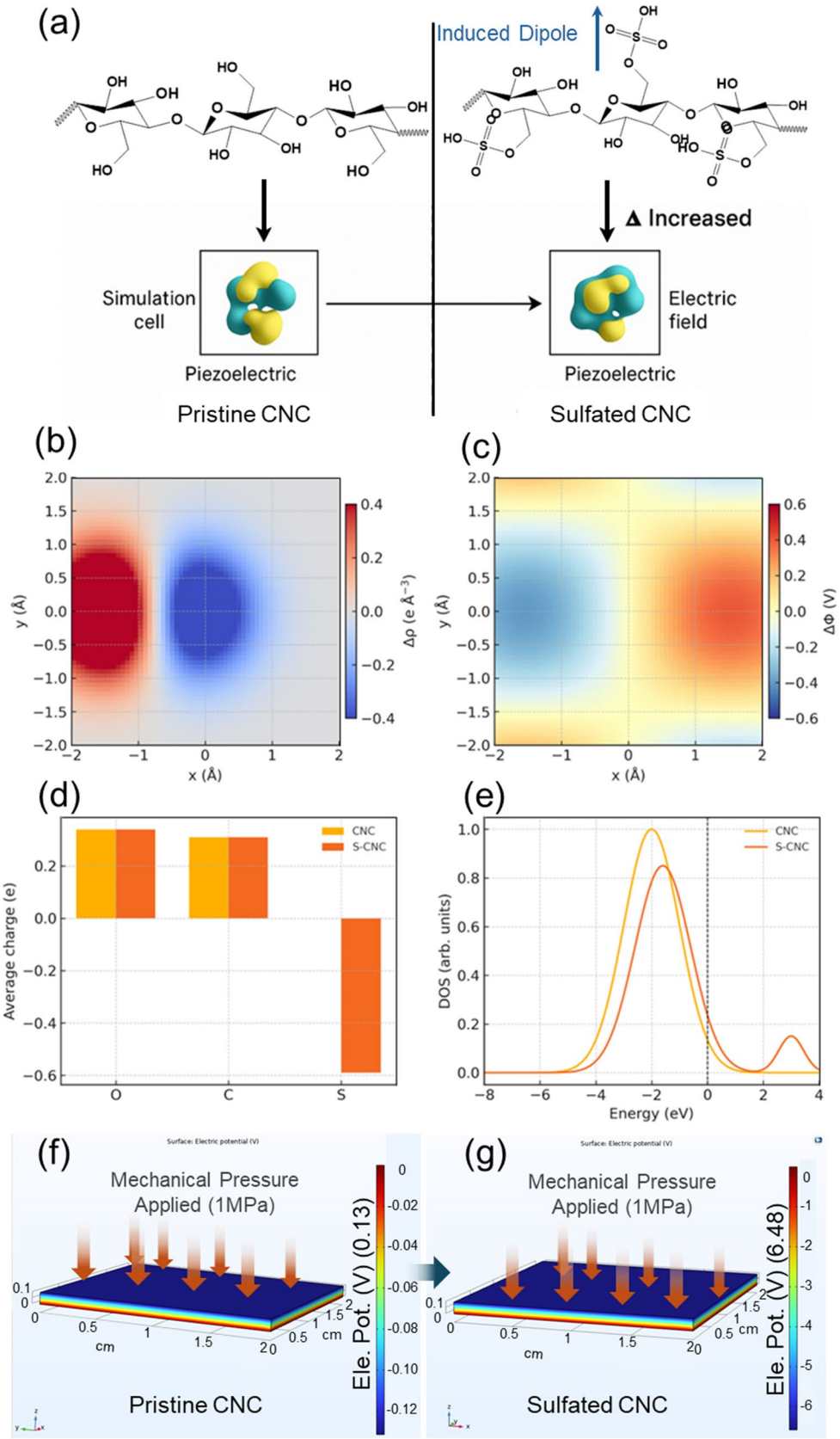

Fig. 2 DFT calculations and COMSOL simulations reveal the enhanced piezoelectric response mechanism in sulfated CNCs. (**a**) Schematic illustration of the sulfation-induced dipole enhancement mechanism. Surface-grafted SO_3^- groups induce electron density redistribution along the cellulose chain, amplifying the intrinsic dipole moment. (**b**) Charge density difference map $\Delta\rho = \rho(SCNC) - \rho(CNC)$ on the (010) crystallographic plane, showing electron accumulation (red) at SO_3^- sites and depletion (blue) along the glucose backbone. (**c**) Electrostatic potential difference ($\Delta\Phi$) map demonstrating the enhanced axial electric field gradient in SCNC. (**d**) Bader charge analysis revealing significant charge transfer (−0.59 e) to sulfur atoms. (**e**) Projected density of states (PDOS) comparison between pristine CNC and SCNC, showing the emergence of sulfate-derived states ~2.8 eV below the conduction band edge. (**f**) COMSOL Multiphysics simulation result of electric potential performance of CNC under mechanical pressure (1 MPa). (**g**) Enhancement in electric potential of SCNC under mechanical pressing of pressure (1 MPa)

dipole behavior, boosting the electric potential to 6.48 V, nearly 50 times higher than pristine CNCs as shown in Fig. 2g. This enhancement can be explained using Gauss's law with nonlinear dielectric and piezoelectric coupling equations, as described in Eqs. (1)–(3).

$$\nabla \cdot D = \rho_v \tag{1}$$

$$D = \varepsilon_0 E + P(E) + P_e(S_{elast}) \tag{2}$$

$$E = -\nabla V \tag{3}$$

The first equation represents Gauss's law for the electric displacement field, the second describes the constitutive relation for the electric displacement field in a nonlinear dielectric with electro-mechanical (piezoelectric) coupling, and the final equation expresses the system in terms of electrostatic potential. The simulated results confirm the novelty of the enhanced dipole moment in the cellulose nanocrystal structure, which substantially increases the electric potential under applied mechanical stress. To evaluate the improvement in electric potential corresponding to mechanical stimuli, simulations were performed both before and after applying the load. As shown in Supporting Information (Figure S3), no electric potential is observed without mechanical pressure, whereas the application of 1 MPa to SCNC induces a distinct electric potential, thereby confirming the piezoelectric nature of the material.

2.3 Piezoelectric energy harvesting performance and application versatility

To assess the piezoelectric response of SCNC, the piezoelectric energy harvesting devices were constructed. The PVA/CNT@SCNC composite was used as active layer, which generate electricity through piezoelectric response. The substrate as mulberry paper enhances flexibility and the presence of PVA in the composite enhances the strong adhesion into mulberry paper that can build a high mechanical strength which reduces the leaking of composite during long-term wearable applications. For piezoelectric energy harvesting measurements, the polyester tape as insulator is used to prevent charge leakage into the surrounding environment to ensure the accurate electrical measurement. The device was securely mounted using insulating tape and PDMS layer and connected to a precision oscilloscope to record the voltage fluctuations under mechanical stimuli (Fig. 3a). First, the piezoelectric performance is systematically evaluated for pristine CNC and SCNC to practically confirm the effective nature of sulfation in CNC network as shown in Fig. 3b. It is strongly understood that the results confirm the effect of acid hydrolysis treatment triggers the dipole behavior in cellulose nanocrystal networks. The pristine CNC device shows the voltage less than 1 V while the SCNC enhanced the voltage more than 6 times of pristine CNCs. Second, the PCS-0.5, PCS-1, PCS-1.5, and PCS-2 device that has weight ratio of 2:1:X (PVA/CNT@SCNC), where X = 0.5, 1, 1.5, and 2 as shown in Fig. 3c. The figure indicates that increasing the SCNC content in the samples from PCS-0.5 to PCS-2 enhances the piezoelectric performance without altering the PVA and CNT composition. This observation strongly supports the correlation between the SCNC content and the improvement in piezoelectric properties. Elaborately, the device with PCS-0.5 of SCNC produced a peak voltage of 2 V, which gradually increased to 6 V at PCS-2. The output voltage is attributed to the high density of sulfate functional groups on CNCs, which facilitate strong dipole polarization under mechanical stimulation. Moreover, the interconnected SCNC network at higher loading improves stress transfer across the material, thereby boosting the charge separation and voltage generation. An immediate piezoelectric response from Fig. 3c shows a rapid and stable voltage response further emphasizes the potential of the prepared device for dynamic fast-responsive sensing and energy-harvesting applications. Moreover, to elucidate the role of CNTs in enhancing electron transport and mechanical integrity within the PCS composite, a comparative study was conducted with and without CNT incorporation. The CNT-free PCS exhibited pronounced brittleness and poor bendability, indicating inferior mechanical robustness, whereas the CNT-integrated PCS maintained excellent flexibility with minimal structural deformation, as shown in Figure S4a. To further evaluate its suitability for wearable applications, tensile testing was performed (Figure S4b), revealing that the CNT-containing PCS demonstrates superior mechanical strength, which facilitates more efficient charge transfer under mechanical deformation through its internal dipolar structure. In addition, electrical conductivity measurements (Figure S4c) show that PCS-2 achieves a conductivity of 1.25×10^{-5} S m^{-1}, consistent with enhanced piezoelectric performance due to the formation of effective conductive pathways by CNTs. In contrast, the CNT-free device exhibits significantly reduced energy harvesting capability, generating a maximum voltage of ~2 V (Figure S4d), which is approximately one-third of that obtained for PCS-2, highlighting the critical role of CNTs in establishing efficient charge transport networks. Furthermore, replacing CNTs with conductive carbon black resulted in a noticeable decline in performance (Figure **S5**), attributed to the inability of carbon black to form continuous conductive pathways. This difference arises from the high-aspect ratio of CNTs, which promotes percolative network formation and minimizes charge trapping, whereas carbon black typically leads to discontinuous conduction pathways.

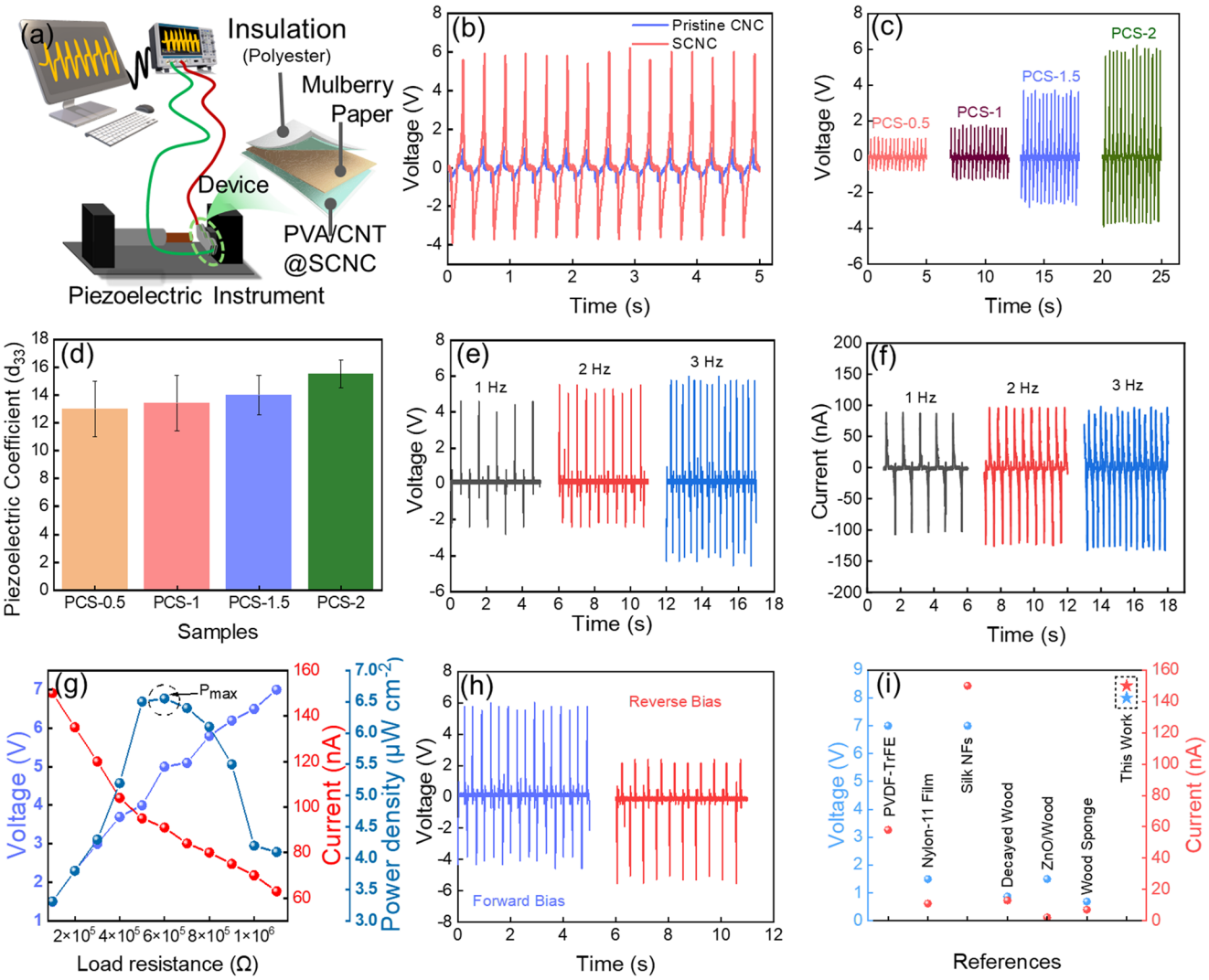

Fig. 3 Piezoelectric measurements performed using PCS and pristine CNC devices. (**a**) Schematic illustration of the device under measurement with a voltmeter attached with a Polyester tape/PDMS layer as insulator. The device combined with an active material as PVA/CNT@SCNC embedded on MP. (**b**) High-piezoelectric response of SCNC compared to pristine CNC. (**c**) Obtained maximum open-circuit voltage performance under different SCNC loading with same PVA/CNT composite (PCS-0.5, PCS-1, PCS-1.5, PCS-2). (**d**) Analysis of Piezoelectric co-efficient with response to different loading content of SCNC (PCS-0.5, PCS-1, PCS-1.5, PCS-2). (**e**) Voltage observed under different frequency conditions of PCS-2 device. (**f**) Output current observed under different frequency conditions of PCS-2 device. (**g**) Maximum power output performance analysis with different resistance load. (**h**) Reversible nature of voltage under forward and reverse bias condition of PCS-2 device. (**i**) Comparison of piezoelectric performance of existing bio-based piezoelectric reports with this proposed work

To further quantify the effect of SCNC loading on piezoelectric properties, the piezoelectric coefficient (d_{33}) was measured for PCS-0.5, PCS-1, PCS-1.5, PCS-2 is shown in Fig. 3d. The d_{33} value increased from ~13 pC/N at PCS-0.5 to ~16 pC/N at PCS-2 indicating a direct correlation between active material and piezoelectric performance. Higher SCNC loading also improves the formation of interconnected domains, facilitating effective stress transfer and stronger polarization. The consistency between the measured d_{33} values and the output voltage further validates the critical role of SCNC content in governing the electromechanical coupling efficiency of the device. The obtained d_{33} values fall within the typical range reported for cellulose-based piezoelectric systems (~5–30 pC N^{-1}), depending on processing conditions and structural organization. These values are also comparable to other biopolymer-based systems and flexible polymers such as PVDF. Although lower than those of conventional piezoceramics, cellulose-based materials exhibit relatively high piezoelectric voltage coefficients (g_{33}) due to their inherently low dielectric constants, making them particularly suitable for energy harvesting applications. Therefore, the performance observed lies well within the expected range for sustainable and flexible piezoelectric materials, as summarized in Table S2 (Supporting

Information). The above two experimental observations in Fig. 3c and d confirm that the PCS-2 device exhibits superior piezoelectric energy-harvesting characteristics compared to other samples, and thus it was selected for subsequent measurements and investigation. In addition, the enhancement of piezoelectric properties upon sulfation of CNC was further validated through dielectric constant measurements of all PCS samples, including pristine CNC (PCS-0), over a range of frequencies. As shown in Figure S6, increasing the degree of sulfation within an otherwise identical PVA/CNT composite results in a noticeable increase in the dielectric constant. This trend indicates enhanced polarization within the material, providing strong evidence that sulfation promotes dipole formation and contributes to improved piezoelectric behavior.

The piezoelectric performance of the PCS-2 device was evaluated under continuous tapping with a force of 40 N to simulate dynamic mechanical excitation. As shown in Figure **S7**, the device generates clear voltage pulses with a maximum output of 6 V with a smaller negative swing of ~−2 V. This asymmetric voltage behavior is attributed to the intrinsic dipole orientation in the SCNC matrix, where compression induces stronger dipole polarization compared to the release phase. The reproducible voltage spikes across multiple tapping cycles confirm the stable and reversible piezoelectric conversion behavior of the device. The sharp positive responses upon tapping demonstrate efficient charge separation, while relatively smaller negative excursions suggest partial charge relaxation during unloading. Such characteristics are desirable for self-powered energy harvesting and sensing applications, where immediate response with consistent pulse signals under mechanical stimuli is very critical. To evaluate the reproducibility of the device performance, five independently fabricated PCS-2 devices were systematically tested, all of which exhibited consistent output characteristics, as shown in Figure S8 (a, b). Furthermore, the long-term operational stability was assessed over 20,000 piezoelectric cycles, during which the device maintained nearly unchanged performance, demonstrating excellent durability and reliability for real-time practical applications (Figure S8c). In addition, the resultant output voltage can be utilized through charge storing techniques using capacitors. Therefore, a 1 μF capacitor is connected to the device under continuous tapping shows the charging ability of capacitors as shown in Figure S9. The capacitor attains the maximum voltage of about 8.3 V within continuous 160 s of tapping (piezoelectric performance). This conveys the proof the device's practical applications ability for wearable energy harvesting applications.

The frequency response of the optimized device was further investigated by applying periodic mechanical stimuli at 1, 2, and 3 Hz is shown in Fig. 3e. At all frequencies, the device generated a clear alternating voltage pulse with a peak-to-peak amplitude of 5–6 V, indicating stable performance irrespective of tapping speed. As the frequency increased, the number of pulses within the same time window increased proportionally clearly indicating the dynamic adaptability of the device to different excitation conditions. It is evident that the voltage amplitude remained nearly constant with frequency indicating that the output is primarily governed by the applied stress rather than the pressing rate. This consistency highlights the robustness of the SCNC matrix in maintaining effective dipole polarization. Such frequency-independent voltage stability is advantageous for practical applications in self-powered sensors, while irregular or rapid human emotions are common. The time-resolved output current under similar different driving frequencies is shown in Fig. 3f. Distinct alternating current peaks were observed during each compression and relaxation cycle, confirming a stable dipole orientation and effective electro-mechanical coupling effect. The figure depicts that as the frequency increased from 1 Hz to 3 Hz, the corresponding output current also enhances due to the higher rate of deformation and increased charge transfer per unit time. The symmetric peak and minimal baseline noise further signifies the high stability and excellent reversibility of the piezoelectric response. Figure 3g signifies clear load-dependent electrical study by investigating the enhancement in voltage with reduction in current output respect to the external load increase, consistent with high-impedance energy harvesters. The power density shows a pronounced maximum Power (P_{max}) in the range of 6.5–7.5 μW cm^{-2} at 5×10^5 Ω indicates the impedance matching and optimal energy extraction. This behavior well confirms stable piezoelectric performance and highlights the device's capability for low-power flexible energy harvesting applications. Figure 3h shows the piezoelectric nature of the device under both forward and reverse bias condition indicates a similar-opposite response. In the forward configuration, the device generates a voltage spike ranging from ~−4 V to 6 V, when the electrodes were reversed, the polarity of the signals inverted correspondingly, while the amplitude of the voltage pulses remained nearly unchanged. The encapsulation of PDMS layer during experimental studies and the reverse effects cannot attributed to any triboelectric effects, thereby validating the dominant piezoelectric mechanism where the direction of induced polarization depends on the electrode orientation. The reproducibility of the output under both forward and reverse electrical connections further confirms the stability and reliability of the device. Notably, the obtained performance surpasses several previously reported bio-derived piezoelectric systems, as illustrated in Fig. 3i [49–54]. A detailed comparison with cellulose- and CNC-based piezoelectric devices is provided in Table S3 (Supporting

Information), highlighting the improved performance of the present system. As described in table S3, the device exhibits similar and slightly higher dielectric constant and figure of merit (FOM) than conventional cellulose based materials.

Furthermore, the environmental stability of the device and its piezoelectric response were evaluated under varying moisture conditions. As shown in Figure **S10**, negligible voltage output was observed when the device was directly exposed to water. In contrast, the device exhibited a gradual recovery of piezoelectric performance with decreasing moisture content, generating ~ 2 V at 40% relative humidity, ~ 4 V under moderately dry conditions, and reaching a maximum output of ~ 6 V in a completely dry state. This behavior highlights the strong dependence of piezoelectric performance on environmental moisture, likely due to the screening effect of water molecules on surface charges and dipole alignment. This suppression of piezoelectric activity under wet conditions might be attributed to the high dielectric constant, which screens the polarized dipoles within the SCNC matrix when contact with water. Moreover, there might be a possibility of attachment of cations in the sulfated groups in the SCNCs which reduces the dipole behavior and leads to the reduction of piezoelectricity.

To investigate the role of sulfate group anchoring in cellulose backbone enhancing the piezoelectric behavior, multiple dip-coating cycles of PCS-2 sample were performed, ranging from zero to three layers. As shown in Figure S11, devices without sulfation showed minimal current generation, whereas those with successive coatings exhibited a stepwise increase in output, reaching 150–200 nA under manually tapping on the device. The fourth coating did not yield any further improvement, indicating that three coatings represented an optimal configuration. The optimized device achieved a peak volumetric power density of 20–40 μW cm^{-2} (Figure S12), surpassing many previously reported flexible piezoelectric systems [55–57]. These results underscore the critical role of sulfation in promoting dipole alignment and enhancing energy conversion efficiency, highlighting the potential of this composite system for use in high-performance, self-powered wearable electronics and energy-harvesting technologies.

Notably, the prepared device exhibited an outstanding sensitivity even under low-intensity mechanical stimuli, highlighting its robust piezoelectric performance and potential for practical implementation. Figure 4 illustrates the real-world applicability of the device across a range of biomechanical energy-harvesting scenarios without any use of conventional instrument-based experiments to ensure various practical adaptability. As a representative example, the device was mounted on a human index finger and was found to successfully capture motion-induced voltage signals during finger bending (Fig. 4a). The corresponding signal fluctuations, supported by Video SV1, demonstrated a high responsiveness to subtle biomechanical movements. This functionality renders the device a promising candidate for use in wearable biomedical systems, enabling the real-time monitoring of patient activity, rehabilitation progresses, and musculoskeletal diagnostics.

The further applicability of the developed system was demonstrated by integrating the device beneath a shoe insole. While walking, the device consistently generated voltage outputs (Fig. 4b and Video **SV2**), confirming its ability to harvest energy from daily human movements. To highlight its versatility, the device was embedded into a keyboard interface by attaching it beneath the spacebar. Each keypress exhibited a clear voltage response (Figs. 4c). Additionally, when integrated across multiple keys (i.e., the c, h, u, n, g, and a keys), devices of different sizes produced distinct signal profiles, offering a foundation for intelligent input encoding. This capability can be leveraged in silent communication systems, emergency signaling, or personalized user interfaces, as discussed in the Supplementary Information, Figure S13.

The high sensitivity of the device to light pressure was further confirmed through repeated hand clenching and release cycles. As shown in Fig. 4d, each motion cycle generated reproducible voltage outputs, indicating the reliable detection of low-force biomechanical events. Building on this, the device was positioned on the wrist to evaluate its capacity for monitoring pulse signals. No response was observed when the device was loosely placed; however, once securely affixed to the skin, clear pulse-induced voltage peaks emerged in the range of 60–70 mV (Fig. 4e). Following physical activity, the voltage amplitude increased to ~ 0.3 V with a shortened signal interval, confirming a strong correlation between the physiological pulse rate and the piezoelectric output. These results highlight the viability of this device for use in wearable health diagnostics and cardiovascular monitoring.

To evaluate the environmental stability of the device, the influence of ambient humidity was systematically assessed. As shown in Fig. 4f, the voltage output exhibited a distinct inverse relationship with an increasing relative humidity (RH), namely from ~ 12 V at 17% RH to ~ 50 mV at 100% RH. This degradation was attributed to moisture-induced screening effects and the disruption of dipole alignment via interactions between the water molecules and the sulfated functional groups. Despite this sensitivity, the device retained its operational functionality across the entire humidity range, confirming its resilience under fluctuating environmental conditions.

Collectively, the demonstrated multifunctionality, environmental adaptability, and high sensitivity to mechanical and physiological stimuli exhibited by the device confirm

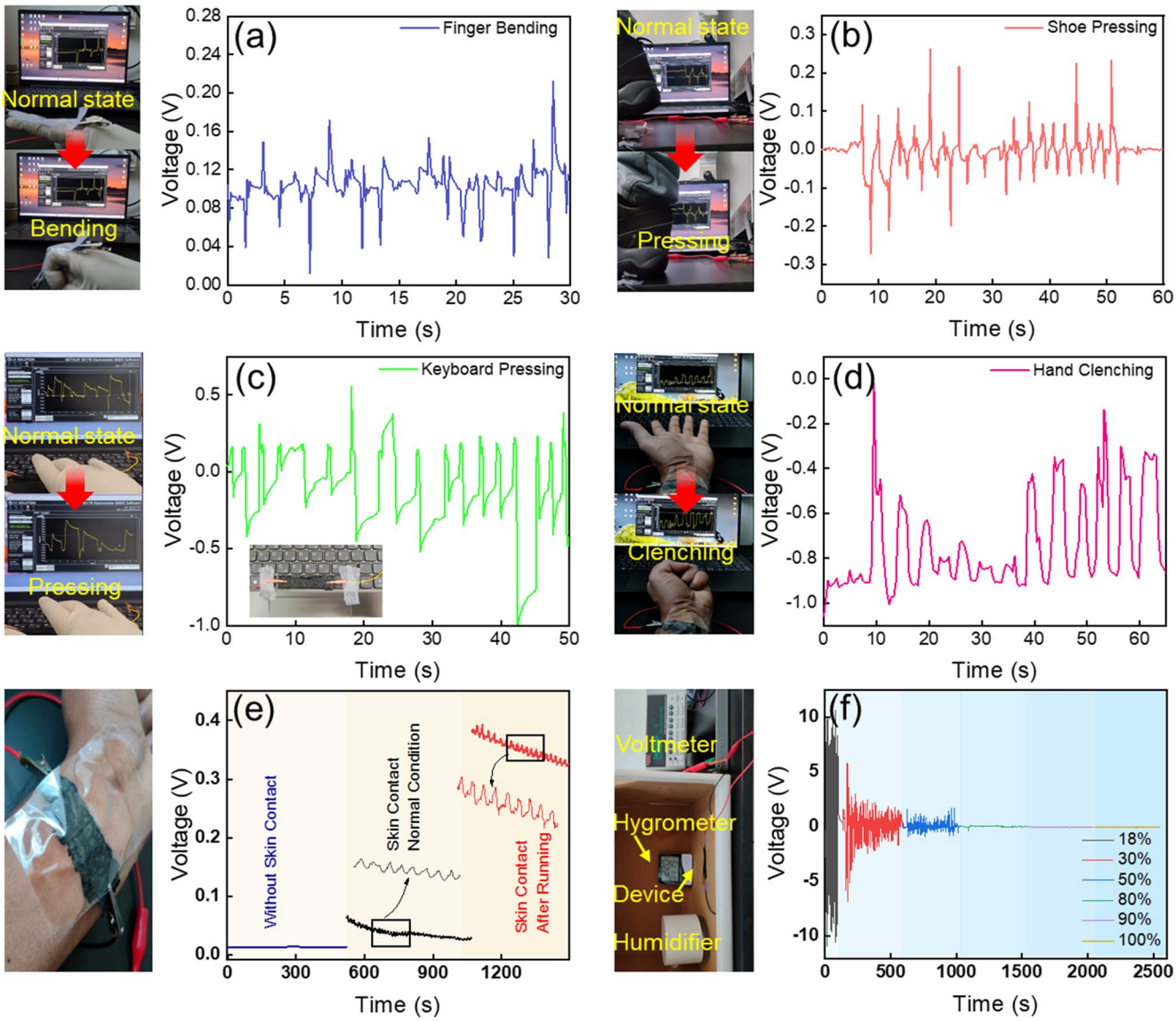

Fig. 4 Energy harvesting performance of the device under different practical conditions (Manual mechanical stimuli) The dimension of the device is (1 cm * 3 cm). (**a**) Voltage generation under index finger bending with various cycles. (**b**) Voltage cycling upon pressing the device with a shoe. (**c**) Change in voltage when pressing the device attached to a keyboard. (**d**) Change in voltage during hand clenching wherein the device is attached to the wrist. (**e**) Highly sensitive nature of voltage generation using the pulse from a human body when the device is securely attached. (**f**) Voltage changes over different relative humidity levels ranging from 18% to 100%

its strong potential for integration into next-generation self-powered systems, including wearable health monitors, biomechanical energy harvesters, and intelligent human–machine interface platforms.

2.4 Strain-sensing performance of the flexible PVA/CNT@SCNC composite device

The deliberate incorporation of PVA into the MP substrate significantly enhanced the mechanical stretchability, conformability, and interfacial adhesion of the composite, enabling the uniform dispersion and stable anchoring of SCNCs within the matrix. These synergistic effects led to the development of a structurally integrated and highly responsive piezoresistive sensing platform capable of detecting subtle and dynamic mechanical deformations with high fidelity. Previous electrical measurements demonstrated the heightened sensitivity of the composite under minimal mechanical perturbation, establishing a strong foundation for its potential in high-resolution strain sensing and next-generation wearable diagnostics. The ultra-flexible and skin-conformable nature of the device allows for stable and comfortable adhesion to various anatomical sites, including the forearm, knee, finger, wrist, and neck, without compromising the signal fidelity or user mobility.

To evaluate the piezoresistive response of the device, strain-sensing tests were conducted by monitoring the relative resistance changes during dynamic human motion, as illustrated schematically in Fig. 5. When mounted on the forearm (Fig. 5a), a rectangular prototype sensor (1.5 × 5 cm) generated sharp, reproducible reduction in resistance fluctuations during repeated bending, with a rapid response time of <0.5 s. Importantly, this indicates an excellent responsiveness to low-intensity biomechanical stimuli. Subsequently, the capability of the sensor to detect larger deformations was examined by mounting it on the knee joint (Fig. 5b). Pronounced and periodic variations in the resistance were observed during walking and squatting, confirming the robustness of the system under macroscale joint motion. Similarly, when the device was mounted on a finger (Fig. 5c), it exhibited highly consistent signal patterns during repetitive 90° flexion cycles, demonstrating excellent mechanical durability and signal repeatability under cyclic strain. The device maintained stable performance over prolonged operation (180 s), as shown in Figure S14, with no observable degradation, confirming its reliability and suitability for real-time wearable sensing applications. Additional performance evaluations were conducted by affixing the sensor to the wrist (Fig. 5d) and to the back of the neck (Fig. 5e). In both cases, the device reliably registered resistance changes corresponding to wrist flexion and head rotation,

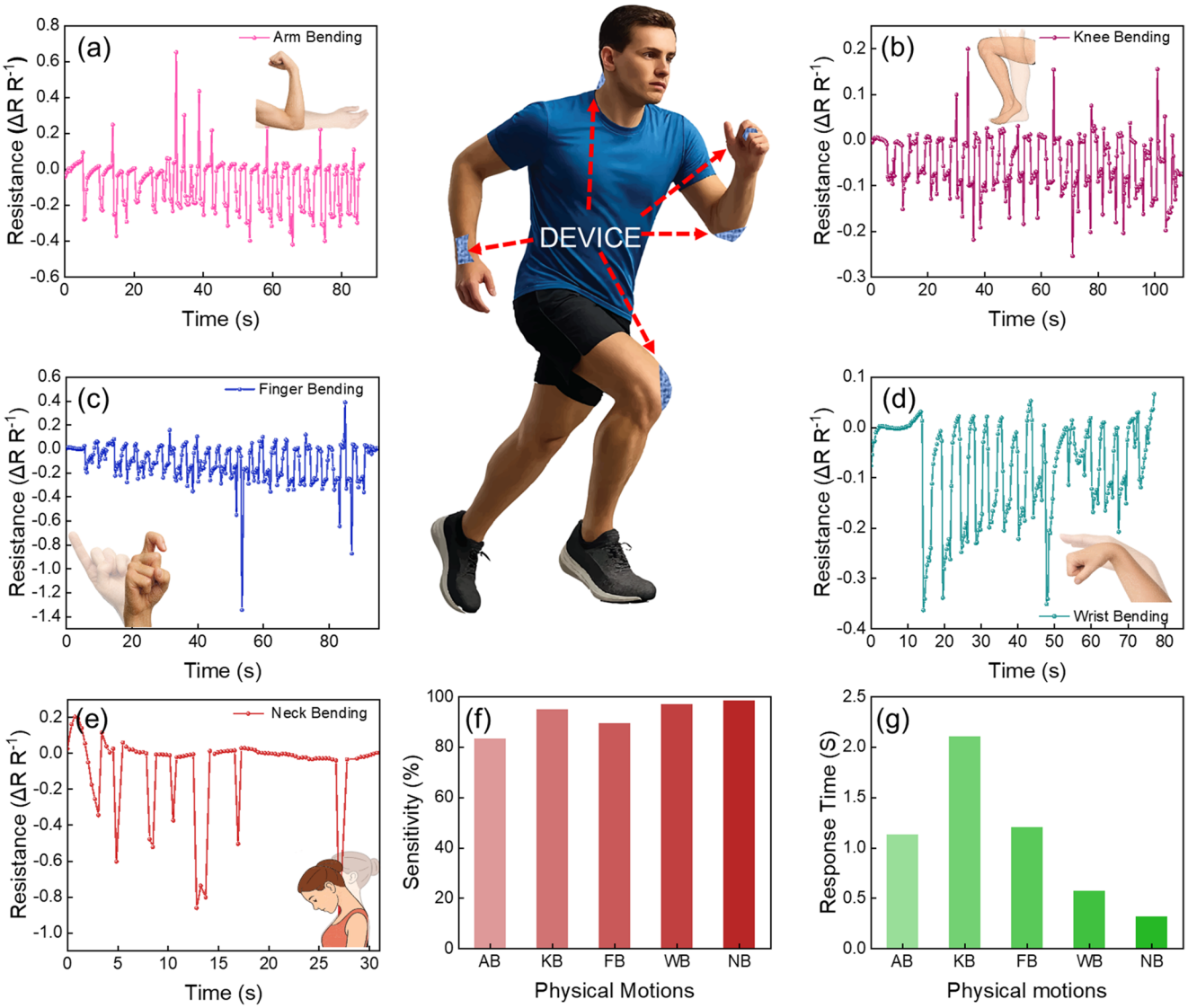

Fig. 5 Strain sensing characteristics of the developed PCS device. (**a**) Relative resistance changes during bending of the arm. (**b**) Relative resistance cycles during knee bending. (**c**) Resistance changes during index finger bending. (**d**) Resistance changes during wrist bending. (e) Resistance changes during neck bending, wherein the device was attached to the neck. (**f**) Sensitivity analysis of the device under Arm bending (AB), Knee bending (KB), Finger bending (FB), Wrist bending (WB), Neck bending (NB). (**g**) Response time of the strain sensor for various physical movements

respectively. The sensitivity of the device to various physiological motions was systematically evaluated to assess its suitability for real-time health monitoring applications, as shown in Fig. 5f. The device exhibits a sensitivity exceeding 80% across different human motions, enabling accurate detection of body movements. Furthermore, the sensitivity of the strain sensor was quantified using the standard gauge factor (GF), as presented in Figure S14b. Although the device demonstrates good sensitivity, it remains lower than that of commercial metallic and semiconductor strain sensors, as summarized in Table S4. However, its performance is superior to that of many recently reported functional material-based sensors, highlighting its competitive advantage [58]. Moreover, all tested physical stimuli elicited rapid responses within a time range of 0.2–2.1 s, as shown in Fig. 5g, meeting the requirements for timely detection in emergency scenarios. The device responsiveness, compared with commercial strain sensors, is summarized in Table S5, indicating that the PCS exhibits faster response than many functionalized composite strain sensors. The response time of the PCS is further compared with commercial strain sensors in Table S6. The PCS demonstrates a response time within the range of 300–1000 ms, which falls within the category of fast strain sensing performance. The combination of high sensitivity and rapid response, in comparison with other composite-based sensors, highlights the device's effectiveness and reliability for real-time wearable sensing applications. Moreover, the performance of power generation under mechanical stimuli and reduction in resistance during straining or bending cycles clearly indicates the device working in a dual performance such as piezoelectric and piezoresistive phenomena which is highly beneficial for various real-time practical applications.

These results validated the mechanical adaptability and conformability of the system across a range of body regions. Detailed visual representations of each test configuration are shown in Figure S15. These results clearly highlight the potential of the flexible composite device for use as a robust and high-resolution strain sensor that is capable of capturing diverse biomechanical signals in real time. Its structural resilience, anatomical versatility, and precise electrical responsiveness render it a promising platform for implementation in motion diagnostics, wearable electronics, and personalized health-monitoring applications. For real-time practical applicability in wearable sensors, a detailed investigation was conducted by analyzing cytotoxicity and biocompatibility, as summarized in Supporting Information Table S7. All materials used in the PCS, including PVA, SCNC, and CNT, exhibit very low toxicity and have been widely employed in various reports on human wearable sensors. Mainly, in this device, the CNTs are embedded within the composite matrix, which is expected to reduce the likelihood of direct exposure during normal use. Moreover, the future direction of this work is to incorporate alternative conductive fillers with zero toxicity with improved piezoelectric performance.

2.5 Demonstration of real-world device applications in sensing applications

Comprehensive experimental validation was subsequently performed to confirm the dual-mode capability of the device as both a piezoelectric energy harvester and a strain-responsive sensor. Building on the results presented in Figs. 4 and 5, additional proof-of-concept demonstrations were conducted to evaluate the feasibility of the device for use in intelligent real-time applications. As illustrated in Fig. 6a, the device was interfaced with an Arduino circuit to demonstrate its practical applicability in healthcare and safety systems. To verify real-time performance, the sensing response was experimentally evaluated and cross-validated under different input frequencies under controlled force (30 N), as shown in Video **SV3**. The device exhibited an immediate response at each frequency, with warning signals indicated by LED illumination, confirming its potential for operation under critical conditions. Furthermore, signal transmission latency and efficiency loss were assessed after integration with the Arduino system. The intrinsic response time of the PCS prior to integration was measured to be 312 mS, which increased to 363 mS after integration, corresponding to a delay of 16.35%. This minimal increase indicates that the device retains near-original performance, supporting its suitability for real-time applications. Additionally, consistent signal behavior across different frequencies suggests that the device operates reliably over a wide frequency range with negligible variation in performance. A detailed force-dependent sensitivity threshold analysis was not included in the present study, as the current experimental setup is limited in precise controlling and quantifying force at the threshold level. This aspect will be addressed in future work. One such scenario targets medical emergency communication for patients with limited mobility or speech capabilities. In this configuration (Fig. 6b), the device was integrated into a hospital bed and connected to an Arduino microcontroller and a buzzer. A gentle tap by the patient produced a detectable piezoelectric signal that was instantly transmitted to the Arduino. The circuit then activated a buzzer to alert caregivers. This application demonstrates the high sensitivity and low-power operating capability of the device, highlighting its potential for use as a noninvasive human–machine interface in critical healthcare environments.

In addition to medical applications, the device was used in a smart doorbell system for home automation and security (Fig. 6c). More specifically, the device was

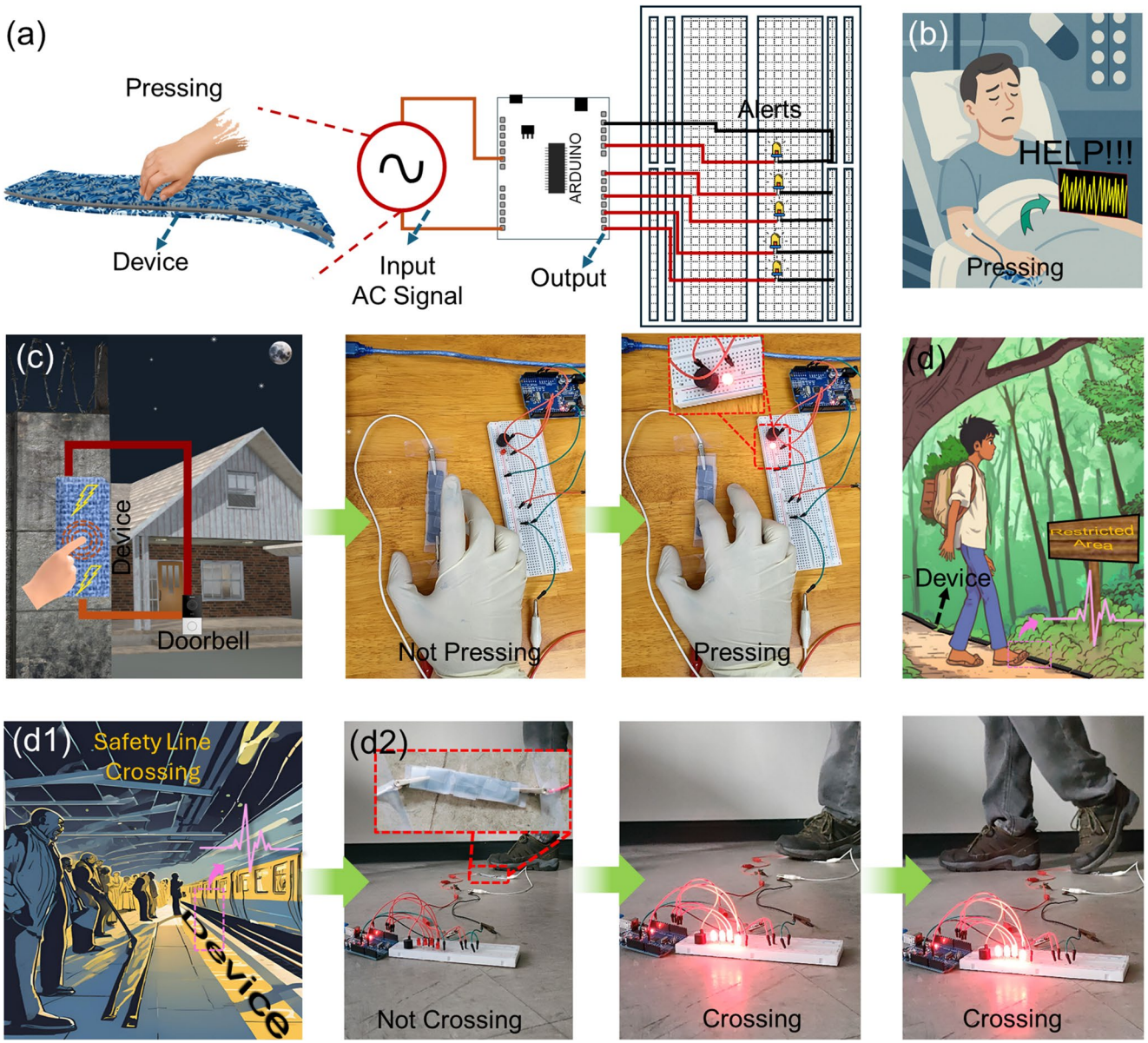

Fig. 6 Practical applications of the device and performance demonstrations. (**a**) Schematic illustration of circuit connection of the device attached to an Arduino circuit and monitoring LEDs as an emergency alarm signal. (**b**) Graphical suggestion of device application as a sensor in the medical field to generate emergency alerts for patients. (**c**) Schematic figure showing application of the device as a sensor for a doorbell system and a practical demonstration of this application. (**d**, **d1**) Graphical images suggesting potential application of the device as a safety line sensor for crossing a defined boundary. (**d2**) Arduino circuit-based practical demonstration experiments showcase the fast-sensing and electricity generating performance of the device when used as a safety line sensor for crossing a defined boundary

embedded in a door frame and connected to an Arduino controlled system equipped with light-emitting diode (LED) indicators and a buzzer. In the standby mode, the system remained inactive. Upon pressing the sensor, a piezoelectric signal was generated, which triggered immediate visual and auditory feedback. Real-time demonstrations, provided in Video SV4, confirm a consistent response time of <1 s. This fast and reliable actuation underscores the suitability of this system for providing smart alerts in safety-critical and accessibility-enhancing applications.

To demonstrate its applicability in public safety and infrastructure monitoring, the device was incorporated into a conceptual safety line detection system designed for restricted zones, such as railway platforms or industrial workspaces. As shown in Fig. 6d, d and d1, the device was embedded on the floor near the designated boundary. When the person stepped across a line, mechanical pressure activated the sensor, producing a voltage signal that was processed by an Arduino microcontroller. The signal simultaneously triggered an LED and a buzzer, providing

real-time audiovisual alerts. This setup simulated boundary violation detection for accident prevention in hazardous environments. Notably, the system was found to remain idle under normal conditions (Fig. 6d) yet responded immediately when the boundary was breached. Repeated trials revealed a consistent performance, as shown in Video SV5. This implementation demonstrates the potential of leveraging the mechanical durability, low-power operation, and sensitivity to localized pressure of the developed sensor for proactive safety applications in both industrial and public infrastructures. These application-specific demonstrations clearly validated the versatility and responsiveness of the composite device, paving the way for its integration into next-generation smart systems focused on healthcare, accessibility, and environmental safety.

3 Conclusion

In summary, we introduced a new material SCNCs into piezoelectricity and strain sensing applications as a mechanically robust, ultra-flexible, and environmentally conscious dual-functional device, which integrates into a single platform. The system was constructed using sulfated cellulose nanocrystals anchored on a mulberry paper substrate and reinforced with carbon nanotubes and polyvinyl alcohol, resulting in a composite structure with excellent electromechanical properties. Based on the theoretical results from DFT and COMSOL Multiphysics, the attachment of sulfate groups into the cellulose backbone enhances the dipole nature of SCNCs which subsequently develops the piezoelectric nature of the specimen when applying mechanical pressure than pristine CNC. From the piezoelectric experimental results, the device exhibited stable open-circuit voltages of 6–8 V and short-circuit currents up to 120–150 nA under mechanical deformation with a power density of 7 μW cm^{-2}. Additionally, the prepared sensor demonstrated a high responsiveness to subtle biomechanical inputs, such as finger bending, wrist pulses, and neck motion, while maintaining outstanding stretchability, conformability, and durability with a sensitivity of more than 80% with a fast response time 0.5–2 s. Furthermore, its piezoresistive behavior enabled precise real-time strain monitoring across various anatomical locations, supporting its applications in motion diagnostics and wearable health monitoring. Beyond its core functionalities, the device was successfully implemented in several real-world scenarios, including medical emergency alert interfaces, smart doorbell systems, and boundary-crossing detection mechanisms for public safety. These demonstrations, realized using simple Arduino-based circuits, highlight the practical utility and rapid response capabilities of the device, in addition to its potential for integration in intelligent human–machine interfaces. By combining multifunctionality, structural flexibility, and sustainable materials, this study established a promising foundation for the development of next-generation piezoelectric sensing technologies. The approach presented herein offers a scalable low-power strategy for future applications in smart healthcare, infrastructure monitoring, and energy-autonomous wearable electronics.

4 Experimental methods

4.1 Synthesis procedure for preparation of the SCNCs

The overview of the material characteristics of the surface-charge-enriched SCNCs and device developmental approach is depicted in Fig. 7, while the detailed procedure is presented in Figure S1. More specifically, sliced raw tissue paper (5 g) was gradually added to sulfuric acid (68 wt%, 10 mL) with continuous stirring at 500 rpm for 4–5 h. The resulting well-dispersed and uniform dark suspension obtained after the reaction was subjected to multiple centrifugation and washing cycles with deionized water and ethanol until a neutral pH (6–7) was achieved. The purified product was dried under ambient conditions for 24 h to obtain the fine SCNC powder.

4.2 Fabrication of the PVA/CNT@SCNC composite on MP

As shown in Figure **S16**, the composite solution was prepared by dissolving PVA (2 g) in deionized water (10 mL) at 80 °C for 2 h, yielding a clear solution. Subsequently, a 1 wt% CNT dispersion (1 mL) was added dropwise, followed by stirring for 1 h to ensure homogeneity. The SCNC powder was then gradually introduced into the PVA/CNT matrix under continuous stirring at 80 °C for an additional 2 h to form a stable, uniformly dispersed composite. Rectangular pieces of MP (1 cm × 2 cm) were immersed in the composite solution for 30 min and air-dried at room temperature (22–25 °C) for 5 h. This dipping–drying process was repeated twice again to ensure a uniform coating and strong interfacial adhesion. An overview of the complete fabrication workflow is shown in Figure S1c. To optimize the material composition, SCNC powder was incorporated in different amounts (x = 0.5, 1, 1.5, 2, and 2.5 g) into a given PVA/CNT matrix with a weight ratio of 2:1:x. The composite containing 2.5 g

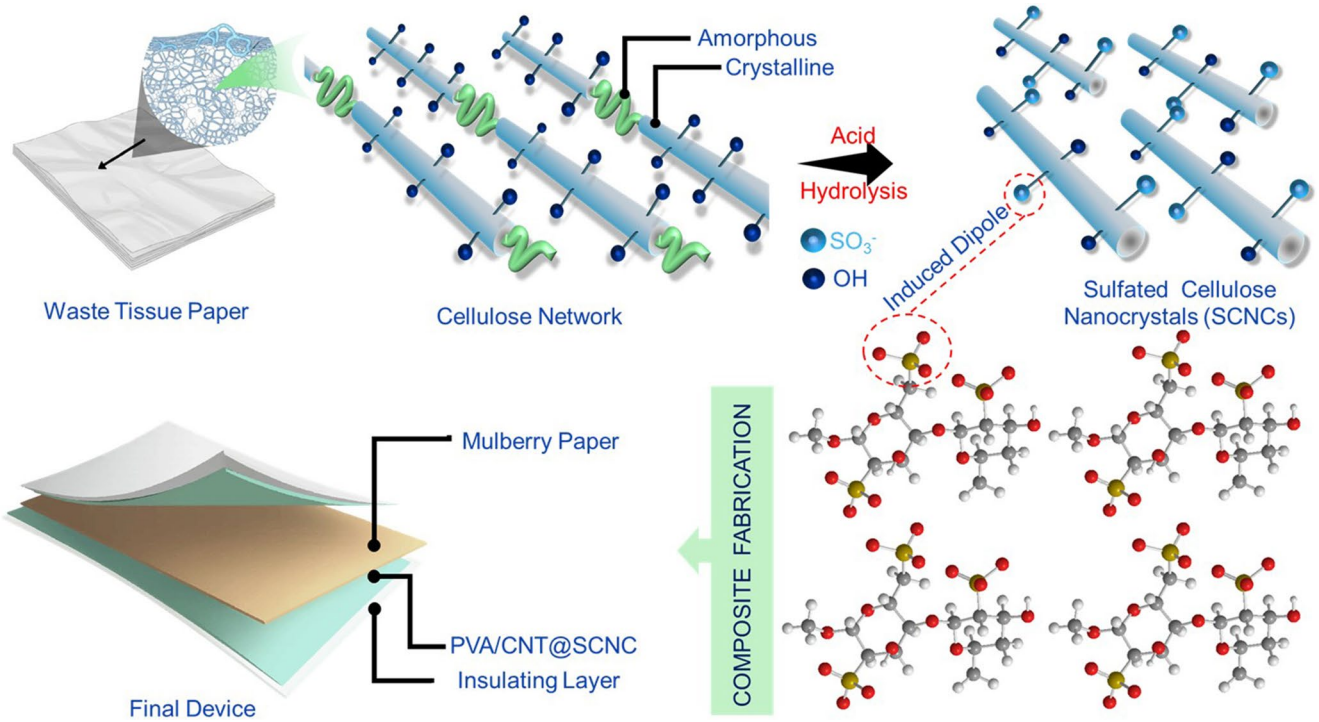

Fig. 7 Schematic illustration of the material characteristics and overview fabrication of the work. Sulfated Cellulose Nanocrystals (SCNCs) obtained from waste tissue paper by acid hydrolysis treatment. The obtained SCNCs reveal an enhancement in dipole behavior by anchoring the sulfate half-ester group into the crystalline network. The flexible device was fabricated by composite material consisting of PVA, CNT, and SCNC on Mulberry paper

SCNC exhibited significant agglomeration and poor coating uniformity on the mulberry paper (MP) substrate; however, to tackle this, we have used surfactants to solve, however, the piezoelectric performance shows very less due to its reducing the dipoles of SCNCs (Figure **S17**), therefore, this composition was excluded from subsequent studies. Accordingly, samples containing 0.5, 1, 1.5, and 2 g SCNC were selected for further characterization. The mass loading of the PVA/CNT@SCNC composite on MP was determined by weight difference before and after coating and drying, yielding loadings of approximately 0.0398 g, 0.0413 g, 0.0453 g, and 0.052 g, respectively. These samples are denoted as PCS-0.5, PCS-1, PCS-1.5, and PCS-2.

4.3 Simulation study using density-functional theory

4.3.1 Model construction

Cellulose Iβ was modelled using a $1 \times 1 \times 2$ supercell (48 atoms, space group $P2_1$) cut along the (010) plane. Three surface hydroxyl groups per chain were replaced with $-SO_3^-/Na^+$ ion pairs to match the experimental sulfur content (≈ 0.32 mmol g^{-1}).

4.3.2 Electronic-structure calculations

Calculations were performed with Quantum ESPRESSO 6.4.1 using PBE-GGA with D3 dispersion corrections. PAW and ultrasoft pseudopotentials were employed with plane-wave cutoffs of 50 Ry (wavefunction) and 400 Ry (charge density). A Γ-centered $2 \times 2 \times 4$ k-point mesh was used. Geometry optimization was conducted until forces were below 3×10^{-4} Ry $Bohr^{-1}$ and energy changes were less than 10^{-7} Ry, with lattice parameters fixed at experimental values (a = 7.86 Å, b = 8.18 Å, c = 10.38 Å).

4.3.3 Properties and post-processing

Charge density differences and electrostatic potentials were computed using pp.x. Bader charge analysis was performed on a $300 \times 300 \times 360$ grid. DOS/PDOS were calculated with 0.05 eV Gaussian smearing. The piezoelectric coefficient d_{33} was determined via Berry-phase method with ±0.5% uniaxial strain.

4.3.4 Numerical accuracy

Convergence tests with increased cutoffs (60 Ry) and k-points ($3 \times 3 \times 5$) showed energy changes ≤ 1 meV/atom and d_{33} variations < 0.03 pm V^{-1}, confirming adequate

convergence. D3 corrections were essential for accurate c-axis lattice parameters.

4.4 Simulation study about COMSOL simulations

4.4.1 Model construction

A rectangular film (2 cm × 2 cm × 0.1 cm) representing either pristine CNC or sulfated CNC (SCNC) was constructed in COMSOL Multiphysics. The model couples the Solid Mechanics and Electrostatics interfaces to simulate the electromechanical response. A uniform mechanical pressure of 1 MPa was applied to the top surface, while appropriate mechanical constraints were applied to prevent rigid-body motion (see Supporting Information for boundary conditions in statement S1). Material parameters for CNC and SCNC—density, relative permittivity (ε_r), Young's modulus (E), and Poisson's ratio (ν)—were specified in the Materials node. Nonlinear dielectric and piezoelectric coupling terms were included where appropriate (see equations in Supporting Information Statement S1). The resulting surface electric potential and field distributions were evaluated to quantify the enhancement in piezoelectric response following sulfation.

4.4.2 Physics interface-multiphysics interface

To analyze the piezoelectric effects in the two materials, CNC and SCNC, a coupled-physics simulation was performed in COMSOL by integrating the Electrostatics (es) and Solid Mechanics (solid) modules. In the Charge Conservation–Piezoelectric Effect section, a uniform pressure of 1 MPa was applied to the top surface of the specimen, while a floating potential boundary condition was assigned to the same surface. To ensure full electromechanical coupling, the entire specimen was defined under a Multiphysics interface combining solid mechanics and electrostatics. This setup enabled the evaluation of the induced surface electric potential (V) generated under mechanical loading.

4.4.3 Meshing and studying

To investigate the piezoelectric response under mechanical stimuli, the entire model was meshed and analyzed using a stationary study condition in COMSOL. A mechanical pressure of 1 MPa was applied to the specimen to evaluate the resulting electric potential distribution. The simulation results reveal that the SCNC specimen exhibits an electric potential approximately 50 times higher than that of CNC under identical mechanical loading, confirming the significant enhancement in piezoelectric behavior induced by sulfation.

4.5 Characterization

The surface morphology of the SCNC/PVA/CNT coated on MP was examined using Field emission scanning electron microscopy (FE-SEM), EVO18, Carl Zeiss. Fourier transform infrared (FTIR) spectroscopy was used to examine the molecular bonding and identification of interactions of functional groups using total reflectance (ATR) mode on a JASCO FT/IR-460+. The material characteristics and the crystallinity of the composite were examined through X-ray diffraction (XRD) analysis using XPERT-PRO X-ray diffractometer. The surface modification and sulphonation after hydrolysis treatment was investigated using X-ray photoelectron spectroscopy (XPS) with an AES module containing Ar-ion and C60 sputtering and further confirmed using Quantax 200 energy dispersive X-ray spectrometer. The piezoelectric properties of the developed all devices were evaluated by encapsulating PDMS layer into the device to avoid any errors using a quasistatic d33 meter (YE2730A, Sinocera Yangzhou, China), while the dielectric constants of all the samples were measured across variable frequencies ranging from 1 kHz to 1 MHz using LCR meter (IM3570, Hioki Nagano Japan). The piezoelectric performance was analyzed by a digital oscilloscope from Keysight (DSOX2912A) from Swindo, UK and the corresponding voltage and current produced by all PVA/CNT@SCNCs were measured using an electrometer (Keithley 2450, Solon, OH, USA). All devices for piezoelectric measurement are sandwiched between the nickel tape with a testing condition applied with a constant applied force of 40 N, with a pressure sensor employed to record the applied force during these measurements. To analyze the tensile strength of the device, Sun scientific Rheometer (Model No: CR-100) is used to check the mechanical strength of device using without and with CNT. For practical application experiments for real-time wearable sensing and smart intelligence, an Arduino UNO board was used. To identify, observe and confirm the structural property of SCNCs leads to piezoelectric nature, DFT simulation was performed using Calculations were performed with Quantum ESPRESSO 6.4.1 and electro-mechanical property was analyzed using COMSOL Multiphysics version 6.2 software.

Supplementary Information The online version contains supplementary material available at https://doi.org/10.1007/s42114-026-01819-2.

Acknowledgements This research was supported by the Global Research Development Center (GRDC) Cooperative Hub Program through the National Research Foundation of Korea (NRF) funded by the Ministry of Science and ICT (MSIT) (RS-2023-00257595). This work was supported by the National Research Foundation of Korea grant funded by the Government of Korea (NRF-RS-2024-00336593).

Author contributions S.L. led the conceptualization and overall study design and performed methodology development, software implementation, data curation, formal analysis, validation, visualization, and investigation. S.L. wrote the original draft and carried out manuscript review and editing. O.P. contributed to software development, data curation, and validation. A.L. contributed to methodology development, validation, and manuscript review and editing. E.W. contributed to investigation, validation, and manuscript review and editing. S.Lim contributed to methodology development, software, data curation, investigation, validation, and manuscript review and editing. B.H. supervised the project, provided resources and funding acquisition, and contributed to methodology, software, data curation, investigation, validation, and manuscript review and editing.All authors approved the final manuscript.

Funding Open access funding provided by Chalmers University of Technology. This research was supported by the Global Research Development Center (GRDC) Cooperative Hub Program through the National Research Foundation of Korea (NRF) funded by the Ministry of Science and ICT (MSIT) (RS-2023-00257595). This work was also supported by the National Research Foundation of Korea grant funded by the Government of Korea (NRF-RS-2024-00336593).

Data availability No datasets were generated or analysed during the current study.

Declarations

Competing interests The authors declare no competing interests.

References

1. Hu J, Dong M (2024) Recent advances in two-dimensional nanomaterials for sustainable wearable electronic devices. J Nanobiotechnol 22:1–20. https://doi.org/10.1186/s12951-023-02274-7
2. Wu J, Teng X, Liu L, Cui H, Li X (2024) Eutectogel-based self-powered wearable sensor for health monitoring in harsh environments. Nano Res 17:5559–5568. https://doi.org/10.1007/s12274-024-6425-8
3. Rana SMS, Wang ZL (2025) Recent advances and prospective strategies for improving the performance of triboelectric nanogenerators. Coord Chem Rev 543:216914. https://doi.org/10.1016/j.ccr.2025.216914
4. Rana SS, Abu Zahed M, Islam MR, Faruk O, Song HS, Jeong SH, Park JY (2023) Metal-organic framework and molybdenum oxide doped highly negative hybridized triboelectric material for self-powered and continuous monitoring of biosignals. Chem Eng J 473:144989. https://doi.org/10.1016/j.cej.2023.144989
5. Man DW, Zhang Y, Tang LP, Xu QH, Chen D, Jiang BD, Han TT, Xu T, Li JB (2024) Nonlinear dynamical characteristics of hybrid tri-stable piezoelectric energy harvester based on rotational motion. Facta Univ Ser Mech Eng 22:257–273. https://doi.org/10.22190/FUME240118033M
6. He JH, Ma J, Alsolami AA, He CH (2025) Variational approach to micro-electro-mechanical systems. Facta Univ Ser Mech Eng 23:649–665. https://doi.org/10.22190/FUME250528023H
7. Li L, Hao M, Yang X, Sun F, Bai Y, Ding H, Wang S, Zhang T (2020) Sustainable and flexible hydrovoltaic power generator for wearable sensing electronics. Nano Energy 72:104663. https://doi.org/10.1016/j.nanoen.2020.104663
8. Ali A, Shaukat H, Bibi S, Altabey WA, Noori M, Kouritem SA (2023) Recent progress in energy harvesting systems for wearable technology. Energy Strateg Rev 49:101124. https://doi.org/10.1016/j.esr.2023.101124
9. Kulkarni MB, Rajagopal S, Prieto-Simón B, Pogue BW (2024) Recent advances in smart wearable sensors for continuous human health monitoring. Talanta. https://doi.org/10.1016/j.talanta.2024.125817
10. Noor-A-Alam M, Kim HJ, Shin YH (2014) Dipolar polarization and piezoelectricity of a hexagonal boron nitride sheet decorated with hydrogen and fluorine. Phys Chem Chem Phys 16:6575–6582. https://doi.org/10.1039/c3cp53971g
11. Milić P, Marinković D, Ćojbašić Ž (2025) Geometrically nonlinear analysis of piezoelectric active laminated shells by means of isogeometric FE formulation. Facta Univ Ser Mech Eng 23:387–405. https://doi.org/10.22190/FUME050123059M
12. Vaghasiya JV, Mayorga-Martinez CC, Pumera M (2023) Wearable sensors for telehealth based on emerging materials and nanoarchitectonics. Npj Flex Electron 7:1–14. https://doi.org/10.1038/s41528-023-00261-4
13. Ali I, Dulal M, Karim N, Afroj S (2024) 2D Material-Based Wearable Energy Harvesting Textiles: A Review. Small Struct 5. https://doi.org/10.1002/sstr.202300282
14. Okechukwu U, Alum EU (2024) Integrating Wearable Health Monitoring Devices with IoT for Enhanced Personal Health Management: A Comprehensive Review. 3:6–10. https://rojournals.org/roj-engineering-and-scientific-research/
15. Han G, Su YF, Ma S, Nantung T, Lu N (2021) Situ rheological properties monitoring of cementitious materials through the piezoelectric-based electromechanical impedance (EMI) approach. Eng Sci 16:259–268. https://doi.org/10.30919/es8d537
16. Lu L, Zhao N, Liu J, Yang B (2021) Coupling piezoelectric and piezoresistive effects in flexible pressure sensors for human motion detection from zero to high frequency. J Mater Chem C 9:9309–9318. https://doi.org/10.1039/d1tc01894a
17. Yuan M, Luo F, Wang Z, Yu J, Li H, Chen X (2023) Smart wearable band-aid integrated with high-performance microsupercapacitor, humidity and pressure sensor for multifunctional monitoring. Chem Eng J 453:139898. https://doi.org/10.1016/j.cej.2022.139898
18. Cornogolub A, Cottinet PJ, Petit L (2016) Hybrid energy harvesting systems, using piezoelectric elements and dielectric polymers. Smart Mater Struct. https://doi.org/10.1088/0964-1726/25/9/095048
19. Zhu M, Liu Q, Wong WY, Xu L (2025) Advancements in Carbon-Based Piezoelectric Materials: Mechanism, Classification, and Applications in Energy Science. Adv Mater 2419970. https://doi.org/10.1002/adma.202419970
20. Choudhury S, Lin Z, Kim S (2026) Biomaterials hydrogel-based piezoelectric materials and devices for implantable bioelectronics. Biomaterials 327:123768. https://doi.org/10.1016/j.biomaterials.2025.123768
21. Hu K, Feng J, Lv N, Jiang W, Lyu Z, Hai Q (2022) Novel flexible piezoelectric-conductive Janus nanofibers integrated membrane

with enhanced pressure sensing performance. J Appl Polym Sci 139:52180. https://doi.org/10.1002/app.52180
22. Fahad M, Waqar A, Park D, Kim B (2025) Flexible MXene/PVDF composite-based piezoelectric device (FPED) for dual applications in energy harvesting and smart IoT-driven gaming. J Ind Eng Chem. https://doi.org/10.1016/j.jiec.2025.02.027
23. Huang Y, Chen S, Li Y, Lin Q, Wu Y, Shi Q (2024) Flexible piezoelectric sensor based on PAN/MXene/PDA@ZnO composite film for human health and motion detection with fast response and highly sensitive. Chem Eng J. https://doi.org/10.1016/j.cej.2024.150997
24. Rana SS, Faruk O, Islam MR, Yasmin T, Zaman K, Wang ZL (2024) Recent advances in metal-organic framework-based self-powered sensors: A promising energy harvesting technology. Coord Chem Rev 507:215741. https://doi.org/10.1016/j.ccr.2024.215741
25. Lotfi R, Naguib M, Yilmaz DE, Nanda J, van Duin ACT (2018) A comparative study on the oxidation of two-dimensional Ti3C2 MXene structures in different environments. J Mater Chem A 6:12733–12743. https://doi.org/10.1039/C8TA01468J
26. Avanish Babu T, Madhuri W (2022) A hybrid microwave sintered PZT composite as a flexible piezoelectric nanogenerator. RSC Adv 12:34454–34462. https://doi.org/10.1039/d2ra05570h
27. Lopez Garcia AJ, Sico G, Montanino M, Defoor V, Pusty M, Mescot X, Loffredo F, Villani F, Nenna G, Ardila G (2021) Low-temperature growth of ZnO nanowires from gravure-printed ZnO nanoparticle seed layers for flexible piezoelectric devices. Nanomaterials. https://doi.org/10.3390/nano11061430
28. Chen J, Li M, Zhu Q, Xiao L, Tang X, Zhou L, Chen X, Chen J, Liu Z, Yuan Q (2024) Flexible BTO piezoelectric generator fabricated by hydrothermal method with the assistance of lignocellulose and carbon nanomaterials. Chem Eng J 497:154742. https://doi.org/10.1016/j.cej.2024.154742
29. Wu Y, Soon PS, Lu JT, Zhou J, Liu YX, Guo Z, Wang K, Gong W (2024) Life cycle assessment of lead-free potassium sodium niobate versus lead zirconate titanate: energy and environmental impacts. EcoMat. https://doi.org/10.1002/eom2.12450
30. Xu S, Hansen BJ, Wang ZL (2010) Piezoelectric-nanowire-enabled power source for driving wireless microelectronics. Nat Commun. https://doi.org/10.1038/ncomms1098
31. Patil TV, Patel DK, Dutta SD, Ganguly K, Santra TS, Lim KT (2022) Nanocellulose, a versatile platform: from the delivery of active molecules to tissue engineering applications. Bioact Mater 9:566–589. https://doi.org/10.1016/j.bioactmat.2021.07.006
32. Csoka L, Hoeger IC, Rojas OJ, Peszlen I, Pawlak JJ, Peralta PN (2012) Piezoelectric effect of cellulose nanocrystals thin films. ACS Macro Lett 1:867–870. https://doi.org/10.1021/mz300234a
33. Pan L, Wang Y, Jin Q, Hu Z, Zhou Z, Zhu M (2024) Self-poled PVDF/recycled cellulose composite fibers utilizing cellulose nanocrystals to induce PVDF β-phase formation through wet-spinning as a flexible fabric piezoelectric sensor. Chem Eng J 479:147742. https://doi.org/10.1016/j.cej.2023.147742
34. Fu R, Chen S, Lin Y, Zhang S, Jiang J, Li Q, Gu Y (2017) Improved piezoelectric properties of electrospun poly(vinylidene fluoride) fibers blended with cellulose nanocrystals. Mater Lett 187:86–88. https://doi.org/10.1016/j.matlet.2016.10.068
35. Wu Y, Ma Y, Zheng H, Ramakrishna S (2021) Piezoelectric materials for flexible and wearable electronics: a review. Mater Des 211:110164. https://doi.org/10.1016/j.matdes.2021.110164
36. Vinayan BP, Zhao-Karger Z, Diemant T, Chakravadhanula VSK, Schwarzburger NI, Cambaz MA, Behm RJ, Kübel C, Fichtner M (2016) Performance study of magnesium-sulfur battery using a graphene based sulfur composite cathode electrode and a non-nucleophilic Mg electrolyte. Nanoscale 8:3296–3306. https://doi.org/10.1039/c5nr04383b
37. Ravi J, Hills AE, Cerasoli E, Rakowska PD, Ryadnov MG (2011) FTIR markers of methionine oxidation for early detection of oxidized protein therapeutics. Eur Biophys J 40:339–345. https://doi.org/10.1007/s00249-010-0656-1
38. Fu J, Liu W, Hao Z, Wu X, Yin J, Panjiyar A, Liu X, Shen J, Wang H (2014) Characterization of a low shrinkage dental composite containing bismethylene spiroorthocarbonate expanding monomer. Int J Mol Sci 15:2400–2412. https://doi.org/10.3390/ijms15022400
39. Kim I-S, Lee B-W, Sohn K-S, Yoon J, Lee J-H (2016) Characterization of the UV oxidation of raw natural rubber thin film using image and FT-IR analysis. Elastomers Compos 51:1–9. https://doi.org/10.7473/ec.2016.51.1.1
40. Radev L, Hristov V, Fernandes MHV, Salvado IMM (2010) Organic/inorganic bioactive materials part IV: in vitro assessment of bioactivity of gelatin-calcium phosphate silicate/wollastonite hybrids. Cent Eur J Chem 8:278–284. https://doi.org/10.2478/s11532-009-0142-8
41. Rozali MLH, Ahmad NH, Isa MIN (2015) Effect of Adipic Acid composition on structural and conductivity solid biopolymer electrolytes based on Carboxy Methylcellulose studies. Am J Sustain Agric 9:39–45
42. Jiang J, Wang X (2019) Adsorption of Hg(II) ions from aqueous solution by thiosemicarbazide-modified cellulose adsorbent. BioResources 14:4670–4695. https://doi.org/10.15376/biores.14.2.4670-4695
43. Zeng S, Fu S, Guo G, Liang H, Qian Z, Tang X, Luo F (2011) Preparation and characterization of nano-hydroxyapatite/poly(vinyl alcohol) composite membranes for guided bone regeneration. J Biomed Nanotechnol 7:549–557. https://doi.org/10.1166/jbn.2011.1316
44. Ramoraswi NO, Ndungu PG (2015) Photo-catalytic properties of TiO2 supported on MWCNTs, SBA-15 and silica-coated MWCNTs nanocomposites. Nanoscale Res Lett. https://doi.org/10.1186/s11671-015-1137-3
45. Rahman MA, Halfar J, Shinjo R (2013) X-Ray Diffraction is a promising tool to characterize coral skeletons. Adv Mater Phys Chem 03:120–125. https://doi.org/10.4236/ampc.2013.31a015
46. Hlady V, Gooch NW (2015) Two surface gradients of polyethylene glycol for a reduction in protein adsorption. Surf Innov 3:172–180. https://doi.org/10.1680/sufi.15.00005
47. Hong S, Yang S, Kim JW, Kim A (2022) Severe carbon accumulation on black phosphorous flakes induced by synchrotron X-ray radiation. Appl Surf Sci 597:153605. https://doi.org/10.1016/j.apsusc.2022.153605
48. Wang J, Mueller DN, Crumlin EJ (2024) Recommended strategies for quantifying oxygen vacancies with X-ray photoelectron spectroscopy. J Eur Ceram Soc 44:116709. https://doi.org/10.1016/j.jeurceramsoc.2024.116709
49. Pi Z, Zhang J, Wen C, Zhang Z, Wu D (2014) Flexible piezoelectric nanogenerator made of poly(vinylidenefluoride-co-trifluoroethylene) (PVDF-TrFE) thin film. Nano Energy 7:33–41. https://doi.org/10.1016/j.nanoen.2014.04.016
50. Wu J, Fu Y, Hu GH, Wang S, Xiong C (2021) Effect of stretching on crystalline structure, ferroelectric and piezoelectric properties of solution-cast nylon-11 films. Polym (Basel) 13:1–12. https://doi.org/10.3390/polym13132037
51. Sun J, Guo H, Ribera J, Wu C, Tu K, Binelli M, Panzarasa G, Schwarze FWMR, Wang ZL, Burgert I (2020) Sustainable and biodegradable wood sponge piezoelectric nanogenerator for sensing and energy harvesting applications. ACS Nano 14:14665–14674. https://doi.org/10.1021/acsnano.0c05493
52. Gao Y, Ram F, Chen B, Garemark J, Berglund L, Dai H, Li Y (2023) Scalable hierarchical wood/ZnO nanohybrids for efficient mechanical energy conversion. Mater Des 226:111665. https://doi.org/10.1016/j.matdes.2023.111665

53. Sun J, Guo H, Schädli GN, Tu K, Schär S, Schwarze FWMR, Panzarasa G, Ribera J, Burgert I (2021) Enhanced mechanical energy conversion with selectively decayed wood. Sci Adv 7:1–8. https://doi.org/10.1126/sciadv.abd9138
54. Sohn C, Kim H, Han J, Lee KT, Šutka A, Jeong CK (2022) Generating electricity from molecular bonding-correlated piezoresponse of biodegradable silk nanofibers. Nano Energy. https://doi.org/10.1016/j.nanoen.2022.107844
55. Kumar A, Das K, Roy A (2024) Improving the energy density and flexibility of PMN-0.3PT based piezoelectric generator by composite designing. Sens Actuators A Phys 376:115609. https://doi.org/10.1016/j.sna.2024.115609
56. Li N, Yang F, Luo T, Qin L (2023) Design and experimental investigation of an ultra-low frequency, low-intensity, and multidirectional piezoelectric energy harvester with liquid as the energy-capture medium. Micromachines. https://doi.org/10.3390/mi14020369
57. Sivakumar A, Deenadayalan E (2024) Design and experimentation of meandered low frequency broadband piezoelectric energy harvester with resonant tuning. JVC J Vib Control. https://doi.org/10.1177/10775463241261845
58. Suryaprabha T, Choi C, Lal S, Seo MY, Kim TW, Wang E, Hwang B (2026) Hierarchical MXene/ZnO Nanorods: WO3/CNT Trilayer Coatings on Cotton for High-Performance Multifunctional Wearable Fabrics. Adv Sci 1–19. https://doi.org/10.1002/advs.202521175